Advanced Steel Construction – Vol. 21 No. 4 (2025) 304–315
DOI:10.18057/IJASC.2025.21.4.3

CYCLIC BEHAVIOR AND SHEAR CAPACITY OF A SINGLE-FRAME MODULAR STEEL STRUCTURE–COLD-FORMED STEEL WALL WITH SEMI-RIGID CONNECTIONS

Qing-Lin Wang [1, 2], Ji-Hong Ye [1, 2] and Ming-Zhou Su [3, 4, *]

[1] *Jiangsu Key Laboratory of Disaster Impact and Intelligent Prevention in Civil Engineering, China University of Mining and Technology, Xuzhou 221116, China*
[2] *Xuzhou Key Laboratory for Fire Safety of Engineering Structures, China University of Mining and Technology, Xuzhou 221116, China*
[3] *School of Civil Engineering, Xi'an University of Architecture and Technology, Xi'an 710055, China*
[4] *Key Lab of Structural Engineering and Earthquake Resistance, Ministry of Education (XAUAT), Xi'an 710055, China*
** (Corresponding author: E-mail: sumingzhou@xauat.edu.cn)*

ABSTRACT

Refined finite element models of a single frame comprising a modular steel structure–cold-formed steel wall (MSS-CFSW) with semi-rigid connections were established using connector parameters calibrated based on shear tests of self-drilling screw connections, then verified against existing test results. The influence of the vertical inter-module semi-rigid connection and steel frame stiffness on the cyclic behavior of the single MSS-CFSW frame was subsequently analyzed. The shear test results indicated that the direction of load relative to the plate edge significantly affected the shear performance of self-drilling screw connections near the edges. The model analysis results indicated that increasing the rotational stiffness and moment capacity provided by the semi-rigid connections increased the initial stiffness of the frame by 31.5% and its shear capacity by 20.2–79.4%; these connections restrained the single frame prior to yielding, but their effects could be disregarded afterwards. Increases in ceiling beam stiffness, floor beam stiffness, and column stiffness increased the shear capacity of the frame by 14.0–41.0%, 15.8–61.1%, and 2.2–6.5%, respectively, and its initial stiffness by 8.1–25.8%, 9.7–21.1%, and 9.9–25.4%, respectively. Finally, the semi-rigid connections were considered equivalent to rotational springs to derive an equation for the shear capacity of a single MSS-CFSW frame with semi-rigid connections and verify it against the numerical simulation results.

ARTICLE HISTORY

Received:	24 November 2024
Revised:	3 January 2025
Accepted:	8 January 2025

KEYWORDS

Semi-rigid connections;
Modular steel structure;
Numerical simulation;
Cyclic behavior;
Cold-formed steel wall

1. Introduction

Given the increasing prominence of uneven construction quality, low efficiency of on-site construction, and serious environmental pollution at construction sites, the traditional construction industry has begun to shift towards industrialization by developing prefabricated buildings. The modular steel structure, which comprises the highest proportion of prefabricated components, is among the most critical approaches for realizing construction industrialization [1].

The walls of a modular steel structure unit are not only a prerequisite for prefabricating its interior but also serve as major lateral resistance members. Given that container construction was a predecessor of modular building systems, a great deal of research on module unit walls has focused on corrugated steel plates. Ding et al. [2,3], Dai et al. [4], and Liu et al. [5] conducted quasi-static tests on one-story and two-story single-span modular steel structures infilled with corrugated steel plate shear walls (CSPSWs), which significantly improved the lateral resistance of modular steel structures. However, the shear stiffnesses of the vertical inter-module connections can be relatively small [6], resulting in a potential mismatch between the stiffness of the module unit and its connections that causes damage to the overall structure. Furthermore, as an independent room, the module unit must provide certain functions such as heat preservation, heat insulation, and sound insulation. However, CSPSWs cannot provide these functions and are difficult to combine with other materials. In addition, the welding of CSPSWs to beams and columns is time-consuming and labor-intensive, making their installation inconvenient during assembly.

The cold-formed steel wall (CFSW) is composed of framing members connected to wallboards by self-drilling screws. Notably, the interior of a CFSW can be filled with relevant functional materials such as thermal insulation materials, and both the CFSWs and steel frame of a module unit can be standardized, produced simultaneously, and assembled in the factory. Furthermore, piping can be pre-embedded inside the CFSW as required, allowing for the full preparation of module units for decoration, plumbing, and electrical requirements. Factory-prefabricated CFSWs can not only be rapidly assembled and erected with high construction quality but are also easy to dismantle and reassemble—a critical characteristic of modular steel structures. Therefore, Wang et al. [7,8] proposed the modular steel structure infilled with cold-formed steel walls (MSS-CFSWs). Fig. 1 shows the novel connection applied between the CFSW and steel frame using high-strength bolts to join connector angles to frame-welded connector plates and self-drilling screws to fix tracks to the connector plates. Test results have confirmed the effectiveness of this connection.

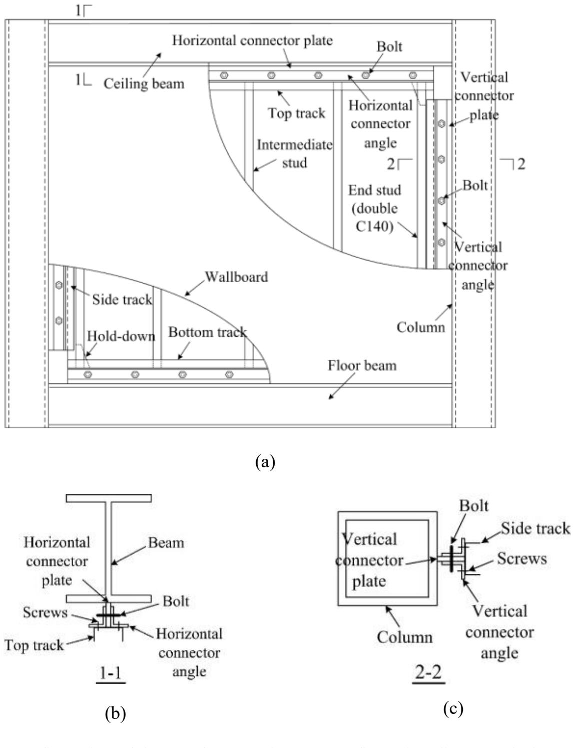

(a)

(b)

(c)

Fig. 1 Configuration of the novel connection: (a) configuration diagram; (b) beam connection; (c) column connection

The unique construction method associated with modular steel structures makes the vertical inter-module connections a critical focus of research. These connections must not only ensure convenience but also provide reliable force transmission. Researchers have accordingly proposed the use of non-welded, interlocking, post-tensioned, and plug-in self-locking inter-module connections [9-14]. As these semi-rigid connections are different from the semi-rigid beam–column joints of traditional steel structures, research into their influence on overall structural performance has been necessary. Chua et al. [15] proposed a horizontal spring model for inter-module connections and reported that the connection modeling method had a significant impact on the performance of the overall structure. Investigations using finite element (FE) models have determined that the horizontal stiffness of the vertical inter-module connections had the greatest impact on structural performance [16], deformation was frequently concentrated in the vertical inter-module connections, the modules remained in the elastic stage, and their displacements were extremely small [6]. Wang and Su [17] derived theoretical equations for the critical buckling load of columns in sway modular steel structures with semi-rigid connections and conducted numerical simulations indicating that the critical buckling load increased with increasing connection rotational stiffness. Indeed, previous studies have indicated that the effects of vertical inter-module semi-rigid connections should be considered when studying the cyclic behavior of a single MSS-CFSW frame. However, owing to test limitations, the boundary conditions of the specimens evaluated in references [7,8] were all hinged; thus, the results did not fully reflect the cyclic behavior of a single MSS-CFSW frame.

Numerical simulations based on refined FE models can improve and expand upon experimental research. A critical aspect of any refined FE model for a single MSS-CFSW frame with semi-rigid connections is the method employed to simulate the self-drilling screw connections. Huang [18], Xu [19], and Yu [20] used nonlinear spring elements to effectively simulate self-drilling screw connections and the corresponding shear performance of the CFSW. The parameters of these elements were generally determined through shear tests of actual self-drilling screw connections. Buonopane et al. [21] conducted numerical simulations indicating that the shear force acting on self-drilling screws can be decomposed into components parallel and perpendicular to the plate edge; the test observations presented in reference [7] confirm this conclusion. However, previous evaluations of self-drilling screw connection shear performance have typically only applied shear force perpendicular to the plate edge. For example, Hao et al. [22], Li et al. [23], and Ye et al. [24] found that, in addition to the wallboard material, a larger distance from the screws to the plate edge increased the shear capacity of the connection. Furthermore, Han [25] evaluated two self-drilling screw connection specimens loaded in shear perpendicular or parallel to the plate edge and reported different shear performances.

Therefore, this study conducted shear tests on self-drilling screw connections and employed the results to develop a refined FE model of a single MSS-CFSW frame in ABAQUS. This model was validated against previous test results, then applied to evaluate the effects of the vertical inter-module connection rotational stiffness and moment capacity as well as beam and column stiffnesses on the cyclic behavior of the frame. Finally, a method for calculating shear capacity of a single MSS-CFSW frame considering the semi-rigid connections was derived and validated against the model results.

2. Shear tests on self-drilling screw connections

2.1. Specimens

Shear tests were conducted on self-drilling screw connections to inform the simulation of their behaviors and determine the parameters of the connector unit. Three types of self-drilling screw connection specimens were designed using different connected plate configurations with the dimensions shown in Fig. 2. These connection specimens joined gypsum or oriented strand board (OSB) to a cold-formed steel plate (CFSP) loaded perpendicular or parallel to its edge (Figs. 2(a) and (c)) with distances from the screws to the plate edge e of 15 mm, 125 mm, and 155 mm. The CFSP was 1.0 mm thick with lengths of L_1 and L_2 at the loaded and fixed ends, respectively; the length of the gypsum or OSB was L_b, its width was W_b, and its thickness was 12 mm. When the shear force was parallel to the plate edge, the constraint effect of the wallboard far from the plate edge on the self-drilling screw connection was considered by taking the W_b of the wallboard as (e+200) mm. A single self-drilling screw was used to connect the wallboard to the CFSP at the loaded end, whereas three self-drilling screws were used for the connection at the fixed end to avoid damage there. Furthermore, a single-screw CFSP to CFSP connection was evaluated as shown in Fig. 2(e).

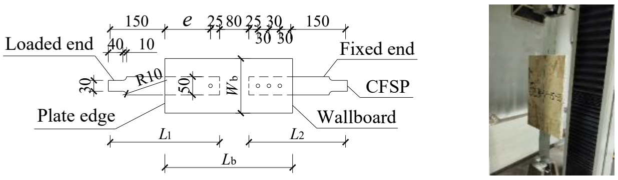

(a)

(b)

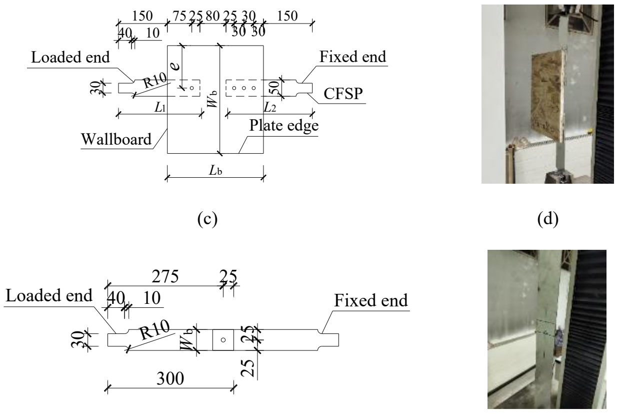

(c)

(d)

(e)

(f)

Fig. 2 Connection details: (a) connection diagram and (b) test setup for shear perpendicular to the plate edge; (c) connection diagram and (d) test setup for shear parallel to the plate edge; (e) connection diagram and (f) test setup for CFSP self-drilling screw connection (units: mm)

Table 1
Shear test specimen parameters

Specimen	Number	e (mm)	L_1 (mm)	L_2 (mm)	L_b (mm)	W_b (mm)
G-V-15	3	15	190	265	235	150
G-V-115	3	115	290	265	335	150
G-V-160	3	160	335	265	380	150
G-H-15	3	15	250	265	295	215
G-H-115	3	115	250	265	295	315
G-H-160	3	160	250	265	295	360
OSB-V-15	3	15	190	265	235	150
OSB-V-115	3	115	290	265	335	150
OSB-V-160	3	160	335	265	380	150
OSB-H-15	3	15	250	265	295	215
OSB-H-115	3	115	250	265	295	315
OSB-H-160	3	160	250	265	295	360
S-SPC-25	3	25	-	-	300	50

All connections were made using 4.8 mm diameter self-drilling screws. The specimen parameters are shown in Table 1. Each connection type was evaluated using different connection materials and e values, and a group of three specimens was tested for each configuration. In the specimen group nomenclature, the first value denotes the connected materials as OSB–CFSP (OSB), gypsum board–CFSP (G), or CFSP–CFSP (S); the second value indicates the connection type with shear acting on the screws perpendicular to the plate edge (V), parallel to the plate edge (H), or on a single self-drilling screw steel plate connection (SPC); and the third value denotes the distance from the screws to the plate edge.

The self-drilling screw connection shear tests were conducted using a 20 kN microcomputer-controlled electronic universal testing machine for loading and data collection as shown in Fig. 2. Each specimen was subjected to a displacement-controlled loading rate of 1 mm/min until it was damaged.

2.2. Failure modes

The failure process of each shear specimen was directly related to its wallboard type, e value, and applied shear direction. Five failure modes were observed, as shown in Fig. 3: plate edge bearing failure (mode B), screw pull-out failure (mode P), plate side pull-out failure (mode SP), OSB delamination tearing failure (mode T), and hole bearing failure (mode HB).

The failure modes of each specimen are reported in Table 2. When e was small (15 mm), the plate edge was prone to cracking under the compression applied by the screw, and the specimens failed owing to damage to the plate edge and side. The specific type of damage depended on the shear direction: when the shear was perpendicular to the plate edge, the specimens exhibited plate edge bearing failure; when the shear was parallel to the plate edge, the specimens failed through the thickness of the plate along its side. In contrast, when *e* was large (125 mm and 155 mm), the plate edge exerted a strong restraining effect on the screw hole, and the specimens were damaged when the self-drilling screws pulled out of the plate regardless of shear direction.

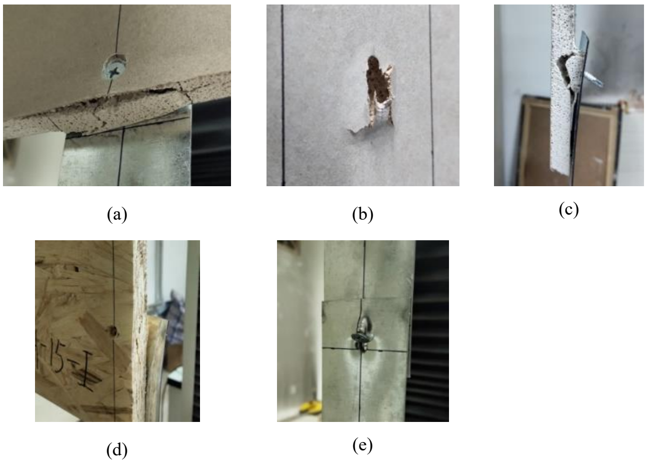
(a) (b) (c)
(d) (e)

Fig. 3 Typical failure modes: (a) plate edge bearing; (b) screw pull-out; (c) plate side pull-out; (d) OSB delamination tearing; (e) hole bearing

Table 2
Characteristic values of shear test specimen skeleton curves

Specimen	Elastic point		Peak point		Failure point		Failure mode
	δ'_e (mm)	P'_e (kN)	δ'_m (mm)	P'_m (kN)	δ'_u (mm)	P'_u (kN)	
G-V-15	0.135	0.128	1.141	0.323	1.384	0.162	B
G-V-125	0.491	0.195	6.128	0.487	14.871	0.243	P
G-V-155	0.528	0.206	5.332	0.516	12.786	0.257	P
G-H-15	0.643	0.198	4.266	0.494	9.320	0.248	SP
G-H-125	0.857	0.209	6.545	0.523	12.580	0.267	P
G-H-155	0.320	0.281	4.760	0.491	11.935	0.246	P
OSB-V-15	1.330	0.756	6.269	1.892	10.628	0.946	B
OSB-V-125	2.339	0.968	12.074	2.422	18.889	1.211	P
OSB-V-155	1.740	0.903	11.351	2.259	13.856	1.195	P
OSB-H-15	2.007	0.887	8.750	2.217	13.181	1.108	T
OSB-H-125	1.509	0.888	9.606	2.221	13.883	1.111	P
OSB-H-155	1.542	0.984	13.024	2.461	17.898	1.230	P
S-SPC-25	2.876	2.929	11.703	7.319	14.478	3.708	HB

2.3. Load–displacement responses

Fig. 4 shows that the load–displacement curves for each group of specimens exhibited obvious ascending and descending segments, but the initial stage of each ascending segment followed an oblique straight line. The curves exhibited strong nonlinearity and the test data possessed a certain degree of discreteness owing to differences among the densities of the boards and specimen fabrication characteristics. The decrease in relative strength from steel to OSB and gypsum board caused the specimen shear capacities to decrease from the S series to the OSB series, then the G series. Notably, each curve for the S series specimens rapidly decreased after reaching its peak, indicating poor ductility resulting from the compression failure of the hole wall; the elastic modulus and stiffness of the connection rapidly decreased once the steel plate entered the plastic stage.

The point with the highest load in the curve was the peak point, and the load and displacement at this point were the peak load P'_m and peak displacement δ'_m, respectively. The elastic point was identified at $0.4P'_m$ in the ascending segment of the curve, and the corresponding load and displacement were the elastic load P'_e and elastic displacement δ'_e, respectively; thus, $P'_e = 0.4P'_m$. To comprehensively reflect the shear performance of each specimen, the point corresponding to $0.5P'_m$ in the descending segment of the curve was taken as the failure point; that is, the failure load $P'_u = 0.5P'_m$, and the displacement at this point was defined as the failure displacement δ'_u. The average test results for the three specimens of each group are listed in Table 2 as the characteristic values of the load–displacement curve for that specimen.

When the shear was perpendicular to the plate edge, the specimen failure mode changed from plate edge bearing failure to screw pull-out failure as *e* increased and the shear capacity increased accordingly. Once *e* exceeded a certain value, the failure mode and shear capacity remained unchanged. Clearly, *e* had a significant influence on the shear capacity of the G series specimen but a relatively small influence on that of the OSB series specimen. When the shear was parallel to the plate edge, *e* had little influence on the shear capacity and peak displacement of any specimen.

When *e* was small, the change in the direction of shear relative to the plate edge was typically accompanied by a change in the failure mode. Furthermore, the shear capacity of the specimen under shear parallel to the plate edge was superior to that under shear perpendicular to the plate edge. When *e* was large, the specimen exhibited screw pull-out failure when subjected to shear in either direction and there was no significant change in the corresponding shear capacity.

A refined FE model of a single MSS-CFSW frame specimen was established by simplifying the experimentally obtained load–displacement curves for the self-drilling screw connections using a multilinear model with reference to [18], as shown in Fig. 5. The peak points in Fig. 4 divide each curve into ascending and descending segments. The initial stage of the ascending segment of each curve was approximated by a diagonal line, but as the damage to the connection specimens intensified, the later stage of the ascending segment exhibited obvious nonlinearity and required a different slope; the elastic point was used to demarcate between these two stages. The overall slope of the descending segment was fairly consistent and was approximated as a single diagonal line with the failure point as its endpoint. Thus, the elastic point, peak point, and failure point were used as the characteristic points of the simplified model.

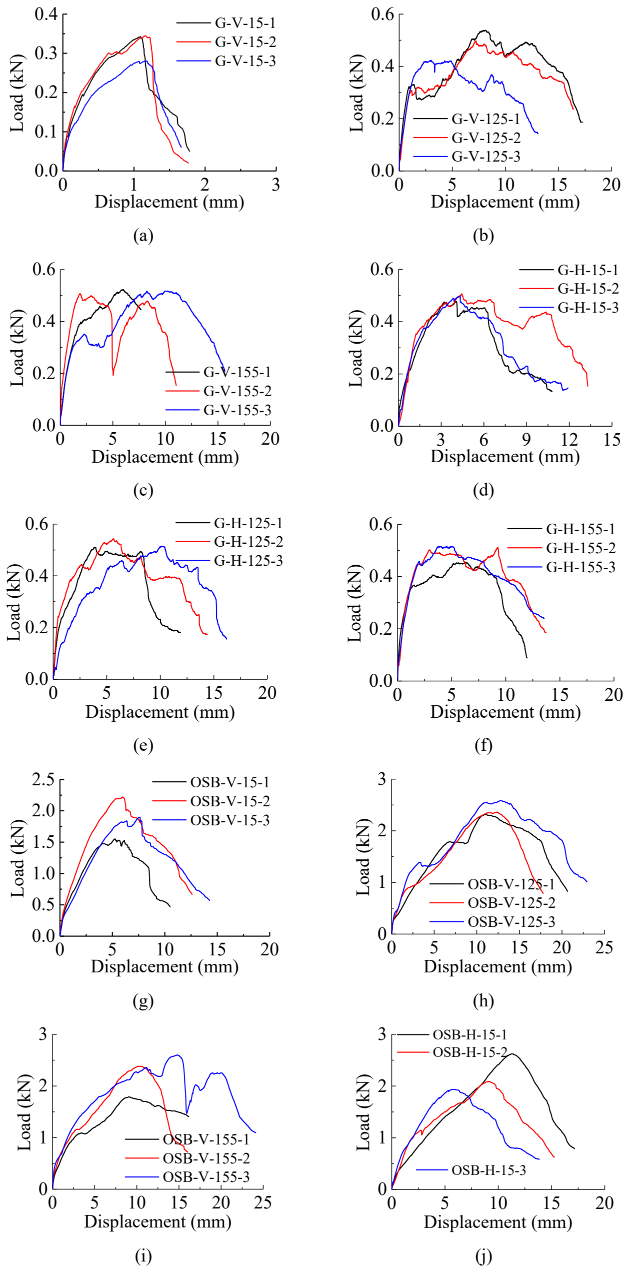

(a) (b)
(c) (d)
(e) (f)
(g) (h)
(i) (j)

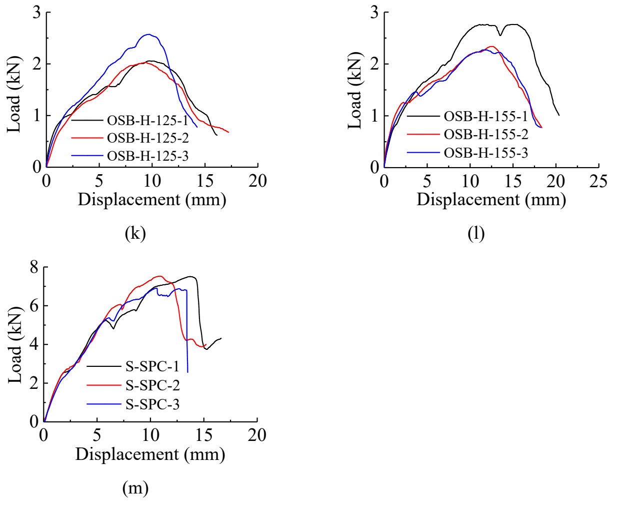

(k)

(l)

(m)

Fig. 4 Curves of the shear test specimens: (a) G-V-15; (b) G-V-125; (c) G-V-155; (d) G-H-15; (e) G-H-125; (f) G-H-155; (g) OSB-V-15; (h) OSB-V-125; (i) OSB-V-155; (j) OSB-H-15; (k) OSB-H-125; (l) OSB-H-155; (m) S-25

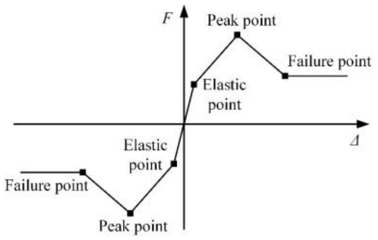

Fig. 5 Simplified load–displacement curve model for self-drilling screw connections

3. FE modeling

3.1. Single-frame substructure of the MSS-CFSW

A short-span single frame from a prototype MSS-CFSW structure was taken as the target substructure. Three full-scale specimens of this substructure were previously designed for cyclic loading tests: two single MSS-CFSW frames and one single steel frame [7]. A refined FE model of specimen MSS-CFSW-1, shown in Fig. 6, was established and validated in this study to investigate the cyclic behavior of a single MSS-CFSW frame with a four-sided connection between the CFSW and steel frame. The specimen details, material properties, test setup, and loading protocol are detailed in reference [7]. The boundary condition of the MSS-CFSW substructure should be semi-rigid, but the existing test setup could not impose the appropriate rotational constraints. Instead, hinge constraints were applied to the top and bottom of each substructure specimen during physical testing with reference to related research [2-5]. The cyclic behavior of a single MSS-CFSW frame under semi-rigid constraints was subsequently analyzed in this study using the refined FE model.

3.2. Model construction

3.2.1. Constitutive model

The steel constitutive model comprised a kinematic hardening model following the von-Mises yield criterion. This model considers the Bauschinger effect, which to some extent influences the performance of steel under cyclic loading. The material properties of the steel in specimen MSS-CFSW-1 were determined by tensile coupon tests as listed in reference [7].

Although gypsum board and OSB are anisotropic materials, studies in reference [18] indicated that both can be assumed to be isotropic in FE models. The stress–strain relationship of the wallboard was described using an ideal elastic–plastic model following the von-Mises yield criterion. The elastic modulus and static bending strength of each wallboard type were determined in previous three-point bending tests [26]. The elastic modulus and bending strength of the OSB were 2347 MPa and 19.8 MPa, respectively, and those of the gypsum board were 2391 MPa and 2.1 MPa, respectively. The Poisson's ratios of the OSB and gypsum board were both 0.2 [27].

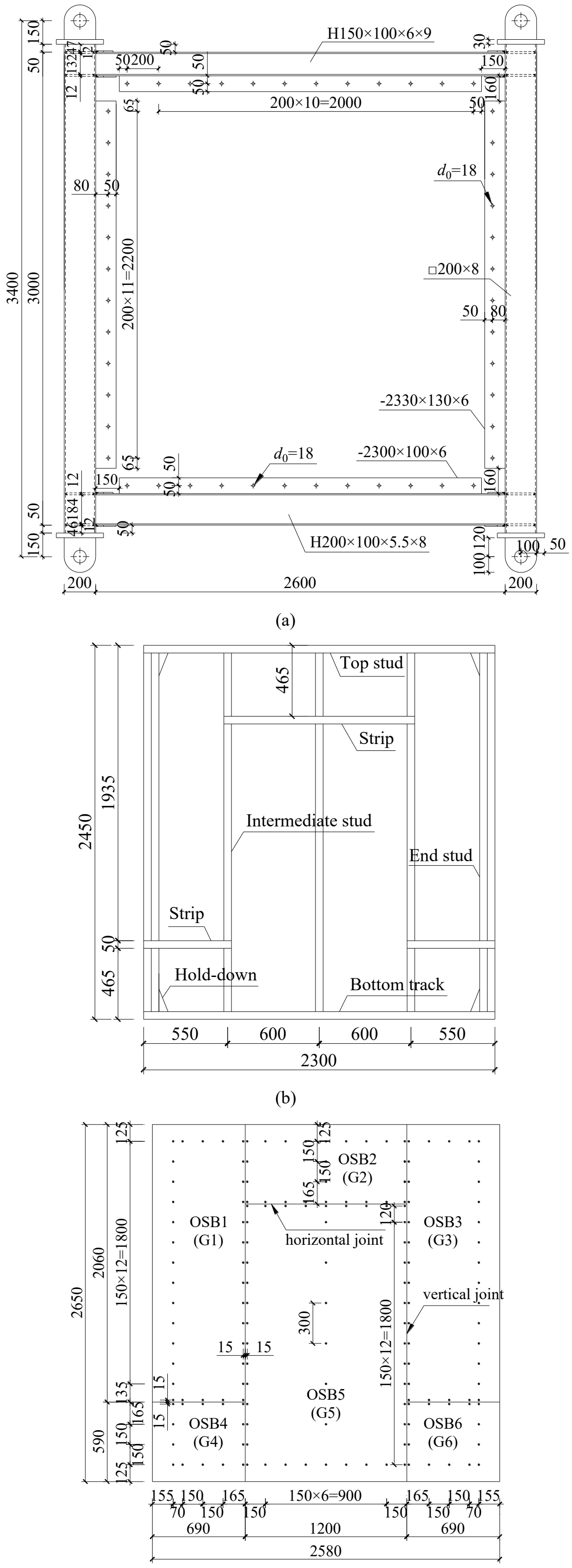

(a)

(b)

(c)

Fig. 6 Details of specimen MSS-CFSW-1: (a) steel frame; (b) framing; (c) wallboards (units: mm)

3.2.2. Element types and meshing

The components of the refined FE model included two columns, one ceiling beam, and one floor beam as well as the necessary cover plates, connector plates, connector angles, angle stiffeners, tracks, studs, strips, and wallboards. As the dimensions of the tracks, studs, strips, and wallboards were much smaller in the thickness direction than in the other directions, they were modeled using S4R shell elements. The remaining components were modeled using C3D8R solid elements with the mesh divided into two layers along the component thickness.

A mesh refinement investigation was conducted to ensure accuracy and computational efficiency. The results indicated optimal element sizes for the column, ceiling beam, floor beam, cover plates, and angle stiffeners of 70 mm, 80 mm, 80 mm, 25 mm, and 20 mm, respectively; the element sizes for the remaining components were all 50 mm. Local refined element meshes of 30 mm and 20 mm were used within 300 mm of the connection regions at the column ends and beam ends, respectively. The final FE mesh results are shown in Fig. 7.

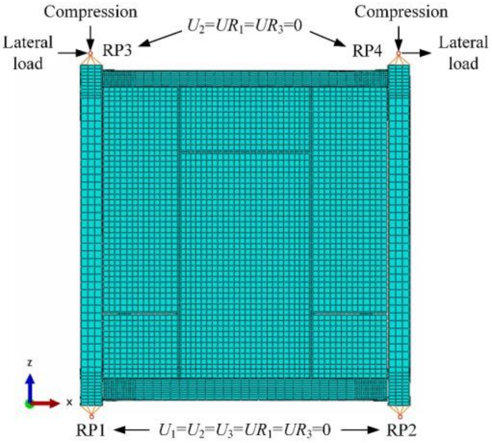

Fig. 7 Mesh and boundary conditions of refined FE model

3.2.3. Interactions

As there was no significant slip between connected components [7,8], computational efficiency was improved by removing the high-strength bolts from the refined FE model and not considering the self-drilling screw connections between the connector angles and tracks or between end stud webs. Instead, a tie constraint was applied to the contact surface between each connector angle and connector plate and each connector angle and track. Furthermore, as all four corners of the CFSW remained undamaged during the test, the FE model was simplified by tying the end faces of each end stud to the webs of the top and bottom tracks to simulate hold-downs. Welds were also simulated using tie constraints, including those between beams and columns, cover plates and flanges, and stiffeners and connector angles. General contact was assigned between wallboard units, wallboard units and framings, and studs and tracks; "hard contact," which transmits pressure while preventing contacting elements from penetrating each other, was applied in the normal direction, and a penalty function, which transmits shear between contacting surfaces, was adopted in the tangent direction using a friction coefficient of 0.4 [28].

3.2.4. Self-drilling screw connection simulation

As the lateral resistance of the CFSW depends on the shear performance of its self-drilling screw connections, accurate simulation of these connections is critical to the refined FE model. ABAQUS connector units were used to simulate the self-drilling screw connections based on the direction of shear relative to the plate edge. The parameters of these units were calibrated according to the relationship between load and displacement along the x and z directions, in the wallboard plane, and the relative rotation of the two points connected by a self-drilling screw was not limited. The self-drilling screw connection was assumed to be rigid in the out-of-plane direction. The in-plane relationship between load and displacement was defined using the simplified model with the characteristic points reported in Table 2.

3.2.5. Boundary conditions and loading

The refined FE model did not include auxiliary test devices such as the loading beam, ground beam, or lateral supports. Instead, reference points were established at the positions corresponding to the pins and were coupled with the top and bottom surfaces of the column. The refined FE model was located in the xoz plane. Three translational degrees of freedom and two rotational degrees of freedom were constrained at the coupling points at the bottoms of the columns such that they could only rotate around the y axis, simulating a hinge, i.e. $U_x = U_y = U_z = UR_x = UR_z = 0$. The out-of-plane translational and rotational degrees of freedom were constrained at the coupling points at the tops of the columns to simulate the presence of the lateral supports, i.e. $U_y = UR_x = UR_z = 0$. The load was applied to the coupling points at the column tops using the same loading protocol applied during the tests: first, a constant vertical load was applied, then the displacement-controlled cyclic lateral load was applied.

Not only were material, boundary, and geometric nonlinearities considered in the refined FE model, but nonlinear connector units were also used to simulate the considerable quantity of self-drilling screw connections. The ABAQUS/Explicit module was accordingly applied to perform quasi-static analysis on the refined FE model considering complex contact and high nonlinearity. Although there was no convergence issue, the computed time increment must be smaller than the stable time increment to obtain stable and reliable results. The stable time increment is often quite small, indicating that the computational efficiency is low. Therefore, the method of defining a fixed time increment, taken as 3×10^{-6} s, was employed to improve computational efficiency. There are two main reasons for choosing a fixed time increment. Firstly, finding suitable time increments for each loading level required significant computational costs. Secondly, using different time increments for different loading levels did not result in a significant decrease in computational cost. The ratio of kinetic energy to internal energy of the model was less than 5%, meeting the requirements for a quasi-static analysis.

3.3. Verification

3.3.1. Hysteretic and skeleton curves

The load–inter-story drift hysteresis and skeleton curves obtained from the refined FE model are compared with the previously obtained test results in Fig. 8. The shape of the numerically simulated hysteresis curve is basically consistent with that of the test curve, though the former appears plumper owing to the use of the simplified multilinear load–displacement curve for the connector units, which cannot accurately reflect self-drilling screw connection slip during unloading, eliminating the pinching phenomenon observed in the test results. The skeleton curves obtained from the numerical simulation and test agreed well, though the refined FE model did not accurately reflect the load degradation process. This occurred because the unloading and reloading paths for the self-drilling screw connections could not be defined using connector units. Indeed, the descending segment of the simplified load–displacement curve only decreased to 50% of the peak load, after which the load carrying capacity remained unchanged. However, note that the load-bearing and energy dissipation capacities of the MSS-CFSWs are respectively provided by the module units and energy dissipation devices. As a result, this study of single MSS-CFSW frames have focused on lateral performance, and the failure of the numerical simulation to accurately capture the energy dissipation capacity of the frame has little impact on this behavior. Therefore, subsequent analyses based on the refined FE model only evaluated the influence of the considered parameters on the skeleton curve, characteristic points, and stiffness degradation of the frame.

A comparison of the peak points obtained from the test and refined numerical simulation is provided in Table 3. The maximum error of peak story drift (θ'_m/θ_m) was relatively large at 13.7%, primarily owing to the occurrence of negative peak loads at different loading levels during the experiments and numerical simulations. The maximum error of peak load (P'_m/P_m), which is of greater concern, was only 2.8%, indicating that the refined FE model accurately reflected the lateral bearing capacity of the MSS-CFSW.

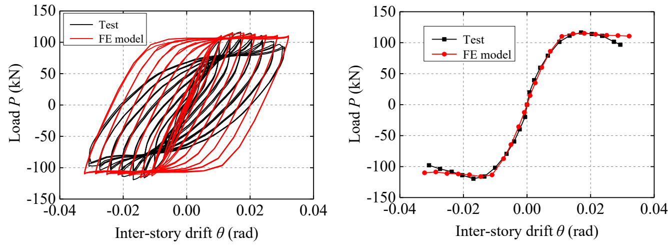

(a) (b)

Fig. 8 Comparisons of (a) hysteretic curves and (b) skeleton curves

Table 3

Peak points obtained by the test and simulation of MSS-CFSW-1

Direction	Test		Refined FE model		Comparison result	
	θ_m	P_m (kN)	θ'_m	P'_m (kN)	θ'_m/θ_m	P'_m/P_m
Positive	0.0170	116.5	0.0180	115.1	1.058	0.988
Negative	-0.0169	-119.5	-0.0145	-116.1	0.863	0.972

3.3.2. Failure characteristics and modes

Fig. 9 compares the failure characteristics of the test specimen with those simulated by the refined FE model. The stress distribution of the refined FE model indicates that the stress in the wallboard unit was concentrated at its corners during the initial loading stage, which is consistent with the observation that the corner self-drilling screw connection was the first to exhibit damage and the wallboard units squeezed against each other during the test. As the load increased, the numerical simulation and test both indicated that the horizontal joints opened owing to the failure of the self-drilling screw connections. Two completely different behaviors occurred at the horizontal strips during both the test and numerical simulation, as shown in Fig. 9 (c): the horizontal strip connected to the gypsum board exhibited almost no deformation, whereas that connected to the OSB exhibited serious out-of-plane deformation.

Fig. 10 compares the specimen failure modes obtained from the test and refined FE model. At the beginning of loading, both the test and model exhibited damage to the self-drilling screw connections at corners of the wallboard units. As the load increased, the wallboard units underwent relative rotation owing to the large number of failed self-drilling screw connections. At the end of loading, the equivalent plastic strain in the refined FE model was primarily concentrated in the flanges at the end of the floor beam, which was consistent with the test-observed local buckling in the floor beam flange. These comparisons confirm that the refined FE model can accurately reflect the specimen failure mode and deformation.

In summary, the refined numerical simulation results agreed well with the test results in terms of the skeleton curve, lateral bearing capacity, failure mode, deformation, and stress distribution. Thus, the refined FE modeling method was confirmed to be effective and it was employed to conduct a parametric analysis on the cyclic behavior of a single MSS-CFSW frame accordingly.

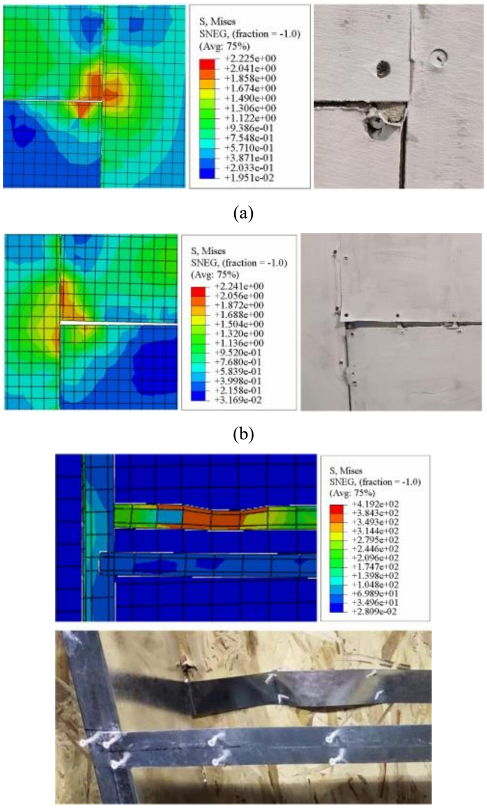

(a)

(b)

(c)

Fig. 9 Comparison of local damage characteristics: (a) corner crushing; (b) horizontal joint opening; (c) strip deformation

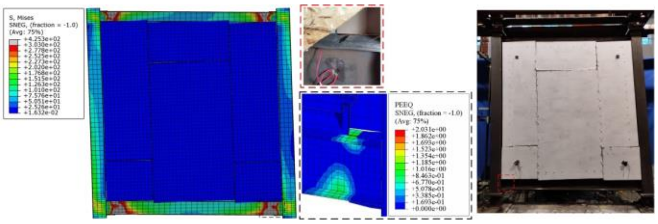

Fig. 10 Comparison of failure mode

4. Parametric analysis

4.1. Model establishment

The refined FE modeling method presented in Section 3.2 was used to establish FE models for parametric analysis. As the verification model was designed to consider a specific test situation, the "Base" parametric analysis model differed from the verification model in the following aspects: (1) The yield strength and tensile strength of the steel were based on the nominal values in GB 50017-2017 [29] and the hardening modulus was 0.01E, where E is the elastic modulus. (2) Given that the vertical inter-module connections in the prototype structure were 150 mm high, the reference points of the parametric analysis model were no longer located at the center point of the pin, but 150 mm away from the top and bottom surfaces of the column. (3) When applying lateral load, the yield displacement Δ_y was first determined by monotonic loading and a displacement-controlled cyclic load was applied accordingly. Before the parametric analysis model yielded, the displacement increment was $0.25\Delta_y$ with one cycle at each loading step; after the parametric analysis model yielded, the displacement increment was $0.5\Delta_y$ with three cycles at each loading step. The parametric analysis model was considered to have failed when the lateral load decreased to 85% of the peak load or the inter-story drift reached 1/30. (4) When investigating the influence of the vertical inter-module semi-rigid connections, the top and bottom surfaces of the each column were coupled to its center point, and the reference point was set 150 mm away from that center point outside the column surface and fixed. A connector unit was subsequently established between the center and reference points, as shown in Fig. 11. During structural design, the moment–rotation curve of each vertical inter-module connection was simplified to an ideal elastic–plastic model with a bias towards safety, as shown in Fig. 12, in which the elastic point of the curve was taken as the critical point between the elastic and plastic stages. The tangent stiffness of the critical point was considered the connection rotational stiffness, and the load corresponding to the critical point was considered the connection moment capacity. Thus, the connection rotational stiffness and moment capacity were defined for the connector unit used to establish the simplified FE model of the inter-module connection in this study; reference [17] verified the effectiveness of this modeling method using experimental data.

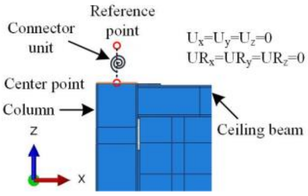

Fig. 11 Diagram of connector unit

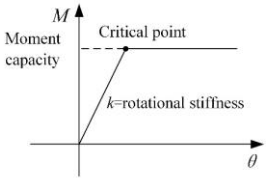

Fig. 12 Simplified model of moment–rotation curve for semi-rigid connections

4.2. Parameter design

4.2.1. Base model

The verified specimen MSS-CFSW-1 model was used as the reference model for parametric analysis, denoted as the "Base" model. The relevant dimensions of each component in the Base model were consistent with those of MSS-CFSW-1, detailed in reference [7], and adjusted according to the requirements in Section 4.1.

4.2.2. Vertical inter-module connection rotational stiffness

The rotational stiffnesses of the vertical inter-module connections at the tops and bottoms of the columns will constrain the rotation of the beam–column joints inside the module unit, thereby affecting its deformation and lateral stiffness. The CRS model series was designed to investigate the influence of the vertical inter-module connection rotational stiffness on the cyclic behavior of a single MSS-CFSW frame with semi-rigid connections. Models CRS-1, CRS-2, and CRS-3 were defined with connection rotational stiffnesses of $0.01R_m$, $0.025R_m$, and $0.05R_m$, respectively, where R_m is the rotational stiffness of the module unit as determined according to reference [29]; the connection moment capacity for each model was $M_{p,cb}$, defined as the full-section plastic bending moment at the end of the ceiling beam, and the other parameters were the same as those of the Base model. The Base model connection rotation stiffness and moment capacity were set to 0.

4.2.3. Vertical inter-module connection moment capacity

The moment capacity also affects the mechanical performance of the vertical inter-module semi-rigid connection and to some extent reflects the constraint of the connections on the module unit. The CMC model series was designed to quantify the influence of the vertical inter-module connection moment capacity on the cyclic behavior of a single MSS-CFSW fame with semi-rigid connections. Models CMC-1, CMC-2, and CMC-3 were defined with connection moment capacities of $0.5M_{p,cb}$, $M_{p,cb}$, and $2M_{p,cb}$, respectively; the Base model connection rotational stiffness and moment capacity were set to 0. The connection rotational stiffness for each model was $0.025R_m$ and the other parameters were the same as those of the Base model.

4.2.4. Ceiling beam stiffness

In addition to transmitting lateral loads to the CFSW, module beams also constrain the deformation of the CFSW. Therefore, the stiffnesses of the module beams will affect their interaction with the CFSW. The CBS model series was designed to investigate the influence of ceiling beam stiffness on the cyclic behavior of a single MSS-CFSW frame with semi-rigid connections. Models CBS-1, CBS-2, and CBS-3 used ceiling beam sections of H140×70×5×7 mm, H220×110×5×7 mm, H240×120×5×8 mm, respectively, corresponding to moments of inertia of 5.171×10^6 mm^4 (0.51I_1), 2.112×10^7 mm^4 (2.09I_1), and 3.053×10^7 mm^4 (3.02I_1), respectively, where I_1 is the moment of inertia of the H150×100×6×9 ceiling beam in the Base model, 1.011×10^7 mm^4. The remaining parameters were the same as those of the Base model.

4.2.5. Floor beam stiffness

The loads acting on the floor beam are often greater than those acting on the ceiling beam; therefore, the cross-section of the former is typically larger. The FBS model series was designed to quantify the influence of floor beam stiffness on the cyclic behavior of a single MSS-CFSW frame with semi-rigid connections. Models FBS-1, FBS-2, and FBS-3 used floor beam sections of H160×80×5×8 mm, H250×125×6×8 mm, and H280×140×6×8 mm, respectively, corresponding to moments of inertia of 8.644×10^6 mm^4 (0.49I_2), 3.570×10^7 mm^4 (2.02I_2), and 5.064×10^7 mm^4 (2.88I_2), respectively, where I_2 is the moment of inertia of the H200×100×5.5×8 floor beam in the Base model, 1.761×10^7 mm^4. The remaining parameters were the same as those of the Base model.

4.2.6. Column stiffness

As the module columns constrain the deformation of the CFSW, their stiffness will affect their interaction with the CFSW. The CS model series was designed to analyze the influence of column stiffness on the cyclic behavior of a single MSS-CFSW frame with semi-rigid connections. Models CS-1, CS-2, and CS-3 used column sections of 160×8 mm, 250×8 mm, and 280×8 mm, respectively, with moments of inertia of 1.878×10^7 mm^4 (0.50I_c), 7.567×10^7 mm^4 (2.00I_c), and 1.074×10^8 mm^4 (2.83I_c), respectively, where I_c is the moment of inertia of the column in the Base model, 3.781×10^7 mm^4. The remaining parameters were the same as those of the Base model.

4.3. Results and discussion

4.3.1. Effects of connection rotational stiffness

Fig. 13(a) shows the skeleton curves of the CRS model series and the characteristic points are listed in Table 4. Since the semi-rigid connections all had the same moment capacity, the peak loads of the three models were basically consistent with each other and significantly higher than that of the Base model. Compared with CRS-1, CRS-2 and CRS-3 both exhibited a 2.4% increase in positive lateral bearing capacity and a 3.9% increase in negative lateral bearing capacity, indicating that the connection rotational stiffness had a limited effect on the lateral bearing capacity. Furthermore, the yield and peak inter-story drifts of CRS-1–CRS-3 generally decreased with the connection rotational stiffness.

Fig. 13(b) shows that the stiffness degradation curves for CRS-1–CRS-3 were consistently above that of the Base model, indicating that semi-rigid connections can strengthen the lateral stiffness of the frame. The initial stiffnesses of the Base, CRS-1, CRS-2, and CRS-3 models were 5.20 kN/mm, 5.59 kN/mm, 6.15 kN/mm, and 6.84 kN/mm, respectively, representing increases of 7.5%, 18.1%, and 31.5% as the connection rotational stiffness increased from 0 to 0.01R_m, 0.025R_m, and 0.05R_m, respectively. This implied that the connection rotational stiffness significantly affected the initial stiffness of the model. Since the connection moment capacities of the three CRS models were the same, the semi-rigid connections of these models successively reached their moment capacities according to connection stiffness. The connections of CRS-3 reached their moment capacities first, where they achieved the maximum constraint of the steel frame before their rotational stiffnesses decreased. Indeed, the stiffness degradation curve of CRS-3 decreased significantly faster than that of CRS-2 or CRS-3. When the connections of CRS-2 reached their moment capacities, the connection rotational stiffnesses of CRS-2 and CRS-3 were both 0, both exhibited the same lateral stiffness (labelled as point A in Fig. 13(b)), and the stiffness degradation laws of the two models were similar, with their curves basically overlapping. When the inter-story drift reached point B in Fig. 13(b), the connection rotational stiffnesses of all three CRS models decreased to 0 and their boundary conditions were the same. At this time, the curves of the three models basically overlapped, as shown in Fig. 13(a).

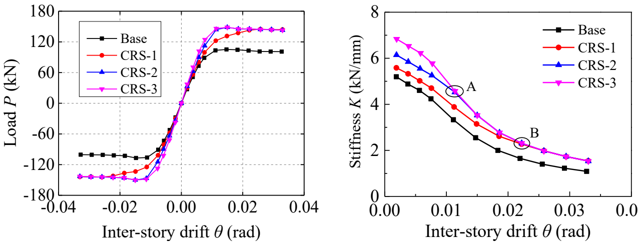

(a) (b)

Fig. 13 CRS model series results: (a) skeleton curves; (b) stiffness degradation curves

Table 4

Characteristic values of CRS model series skeleton curves

Model	Direction	Yield point		Peak point		Failure point	
		θ_y	P_y (kN)	θ_m	P_m (kN)	θ_u	P_u (kN)
Base	Positive	0.0075	88.9	0.0147	105.3	0.0327	100.9
	Negative	-0.0075	-90.9	-0.0148	-107.0	-0.0328	-100.5
CRS-1	Positive	0.0112	122.3	0.0258	145.0	0.0330	144.2
	Negative	-0.0113	-124.7	-0.0259	-144.5	-0.0331	-143.9
CRS-2	Positive	0.0076	112.4	0.0150	148.5	0.0330	142.9
	Negative	-0.0077	-114.6	-0.015	-150.1	-0.0331	-143.1
CRS-3	Positive	0.0077	124.5	0.0150	148.5	0.0330	142.9
	Negative	-0.0077	-127.4	-0.015	-150.2	-0.0331	-143.1

4.3.2. Effects of connection moment capacity

The skeleton curves of the CMC model series are given in Fig. 14(a) and the corresponding characteristic points are listed in Table 5. The lateral bearing capacity significantly increased with increasing connection moment capacity, which can be attributed to the fact that the semi-rigid connections carried part of the lateral load. When the connection moment capacity increased from 0 to 0.5$M_{p,c}$, $M_{p,c}$, and 2$M_{p,c}$, the positive lateral bearing capacities of CMC-1, CMC-2, and CMC-3 increased by 20.2%, 42.0%, and 77.8%, respectively, and their negative lateral bearing capacities increased by 20.2%, 38.3%, and 75.5%, respectively. In addition, the presence of semi-rigid connections improved the ability of the model to resist lateral loads, with the yield load, yield drift, and peak drift generally increasing to varying degrees with the connection moment capacity.

The stiffness degradation curves of the CMC model series are shown in Fig. 14(b), indicating that the initial stiffnesses of the CMC-1–CMC-3 models were obviously larger than that of the Base model. This occurred because the tops and bottoms of the columns in the Base model were hinged with a connection rotational stiffness of 0, whereas the connection rotational stiffnesses of CMC-1–CMC-3 were 0.025R_m. Thus, the higher constraint of the connections on the steel frame generally increased the initial stiffness. However, the initial stiffnesses of CMC-1, CMC-2, and CMC-3 were 6.14 kN/mm, 5.97 kN/mm, and 5.97 kN/mm, respectively, with the latter two stiffnesses both 2.8% smaller than that for CMC-1, indicating that the specific connection moment capacity had little effect on the initial stiffness. Given that the semi-rigid connections of

CMC-1–CMC-3 were all elastic during the initial loading stage, the constraint effect of the connections on the steel frame was the same. Furthermore, the stiffness degradation trends of the three models were consistent, with the corresponding curves basically overlapping. As the load increased, the semi-rigid connections of CMC-1 reached their moment capacities first, their constraint on the steel frame achieved its limit, and the corresponding stiffness degradation curve decreased significantly faster than those for CMC-2 and CMC-3. The stiffness degradation curve of CMC-2 also rapidly decreased once its semi-rigid connections reached their moment capacities. Finally, the stiffness degradation laws of all three models were basically the same in the late stage of loading when the semi-rigid connections reached their moment capacities.

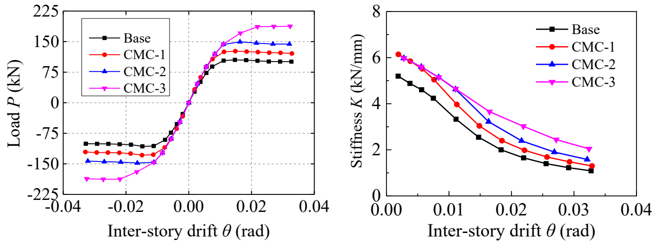

(a) (b)

Fig. 14 CMC model series results: (a) skeleton curves; (b) stiffness degradation curves

4.3.3. Effects of ceiling beam stiffness

Fig. 15(a) shows the skeleton curves of the CBS model series and Table 6 lists their characteristic points. The lateral bearing capacity of the model and initial slope of the skeleton curve increased with increasing ceiling beam stiffness; the former was caused by the corresponding increase in plastic bending moment. Compared to model CBS-1, the positive lateral bearing capacities of the Base, CBS-2, and CBS-3 models increased by 14.3%, 31.9%, and 41.0%, respectively, while their negative lateral bearing capacities increased by 14.0%, 31.0%, and 39.8%, respectively. Furthermore, the yield load, yield drift, and peak drift of the models generally increased with increasing ceiling beam stiffness. However, once the ceiling beam stiffness increased to a certain limit, the yield drift and peak drift no longer increased and the rate of increase in the yield load slowed significantly.

Fig. 15(b) shows that the stiffness degradation curves of the CBS model series were similar, following the same stiffness degradation law. The stiffness degradation rates all changed slowly, then rapidly before remaining flat. The stiffness degradation curves increased from the CBS-1 to Base, CBS-2, and CBS-3 models, indicating that the lateral stiffness of the model increased with increasing ceiling beam stiffness. The initial stiffnesses of the CBS-1, Base, CBS-2, and CBS-3 models were 4.81 kN/mm, 5.20 kN/mm, 5.82 kN/mm, and 6.05 kN/mm, respectively, representing increases of 8.1%, 21.0%, and 25.8% as the stiffness increased from $0.51I_1$ to I_1, $2.09I_1$, and $3.02I_1$, respectively. The initial stiffness increase in CBS-3 was significantly smaller than that in CBS-2, indicating that the ceiling beam stiffness provided limited improvement to the initial stiffness of the model.

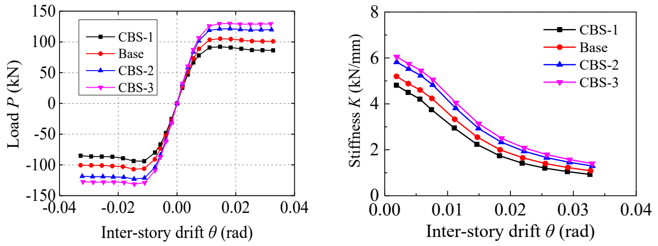

(a) (b)

Fig. 15 CBS model series results: (a) skeleton curves; (b) stiffness degradation curves

Table 5

Characteristic values of CMC model series skeleton curves

Model	Direction	Yield point		Peak point		Failure point	
		θ_y	P_y (kN)	θ_m	P_m (kN)	θ_u	P_u (kN)
Base	Positive	0.0075	88.9	0.0147	105.3	0.0327	100.9
	Negative	-0.0075	-90.9	-0.0148	-107.0	-0.0328	-100.5
CMC-1	Positive	0.0076	107.3	0.0148	126.6	0.0328	120.9
	Negative	-0.0076	-109.7	-0.0149	-128.6	-0.0329	-120.8
CMC-2	Positive	0.0083	119.8	0.0163	149.5	0.0321	144.0
	Negative	-0.0084	-123.0	-0.0164	-148.0	-0.0322	-143.1
CMC-3	Positive	0.0110	144.2	0.0271	187.2	0.0323	186.8
	Negative	-0.0111	-146.4	-0.0272	-187.8	-0.0325	-186.6

Table 6

Characteristic values of CBS model series skeleton curves

Model	Direction	Yield point		Peak point		Failure point	
		θ_y	P_y (kN)	θ_m	P_m (kN)	θ_u	P_u (kN)
CBS-1	Positive	0.0066	72.6	0.0147	92.1	0.0327	86.3
	Negative	-0.0056	-66.6	-0.0111	-93.9	-0.0328	-85.1
Base	Positive	0.0075	88.9	0.0147	105.3	0.0327	100.9
	Negative	-0.0075	-90.9	-0.0148	-107.0	-0.0328	-100.5
CBS-2	Positive	0.0074	101.6	0.0180	121.5	0.0322	119.9
	Negative	-0.0075	-103.9	-0.0146	-123.0	-0.0323	-118.5
CBS-3	Positive	0.0075	106.8	0.0179	129.9	0.0319	129.3
	Negative	-0.0074	-108.1	-0.0145	-131.3	-0.0320	-127.5

4.3.4. Effects of floor beam stiffness

Fig. 16(a) shows the skeleton curves of the FBS model series and the corresponding characteristic points are listed in Table 7. The lateral bearing capacity of the model and initial slope of its skeleton curve increased as the floor beam stiffness increased. Indeed, compared with model FBS-1, the positive lateral bearing capacities of the Base, FBS-2, and FBS-3 models increased by 16.4%, 42.4%, and 61.1% respectively, and their negative lateral bearing capacities increased by 15.8%, 38.0%, and 56.2% respectively, indicating that the increasing the floor beam stiffness significantly improved the lateral bearing capacity of the model. Indeed, the floor beam stiffness had a greater impact on lateral bearing capacity than the ceiling beam stiffness. In addition, the yield drift, yield load, and peak drift generally increased with the floor beam stiffness.

The stiffness degradation curves of the FBS model series are shown in Fig. 16(b). Similar to the influence of ceiling beam stiffness on lateral stiffness, each model exhibited the same stiffness degradation law. The stiffness degradation curves increased from the FBS-1 to Base, FBS-2, and FBS-3 models. The initial stiffnesses of the FBS-1, Base, FBS-2, and FBS-3 models were 4.74 kN/mm, 5.20 kN/mm, 5.49 kN/mm, and 5.74 kN/mm, respectively, representing increases of 9.7%, 15.8%, and 21.1% when the floor beam stiffness increased from $0.49I_2$ to I_2, $2.02I_2$, and $2.88I_2$, respectively. Clearly, the initial stiffness gradually increased with the floor beam stiffness.

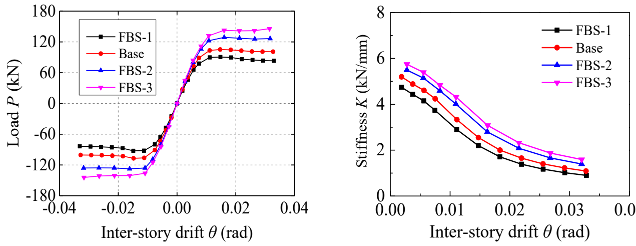

(a) (b)

Fig. 16 FBS model series results: (a) skeleton curves; (b) stiffness degradation curves

Table 7
Characteristic values of CBS model series skeleton curves

Model	Direction	Yield point		Peak point		Failure point	
		θ_y	P_y (kN)	θ_m	P_m (kN)	θ_u	P_u (kN)
FBS-1	Positive	0.0074	77.5	0.0148	90.5	0.0330	83.2
	Negative	-0.0074	-78.8	-0.0149	-92.4	-0.0331	-83.6
Base	Positive	0.0075	88.9	0.0147	105.3	0.0327	100.9
	Negative	-0.0075	-90.9	-0.0148	-107.0	-0.0328	-100.5
FBS-2	Positive	0.0082	106.2	0.0161	128.9	0.0317	126.5
	Negative	-0.0082	-108.7	-0.0161	-127.5	-0.0318	-125.9
FBS-3	Positive	0.0108	132.1	0.0315	145.8	0.0315	145.8
	Negative	-0.0109	-136.1	-0.0317	-144.3	-0.0317	-144.3

4.3.5. Effects of column stiffness

Fig. 17(a) shows the skeleton curves of the CS model series and the corresponding characteristic points are listed in Table 8. All skeleton curves were relatively close to each other, and the lateral bearing capacities of the models remained basically unchanged as the column stiffness increased. Equations (28)–(31) in reference [7] indicate that the lateral bearing capacity of a steel frame primarily depends on the cross-sectional dimensions of its ceiling and floor beams, whereas increasing the cross-sectional areas of its columns cannot improve its lateral bearing capacity. Indeed, compared with model CS-1, the positive lateral bearing capacities of the Base, CS-2, and CS-3 models increased by 2.3%, 5.1%, and 6.5%, respectively, and their negative lateral bearing capacities increased by 2.2%, 5.0%, and 6.5%, respectively. The yield drift and peak drift for each model were basically the same, but the yield load increased significantly with the column stiffness.

Fig. 17(b) shows the stiffness degradation curves of the CS model series, indicating that the influence of the column stiffness on the lateral stiffness of the model can be divided into two stages. Before plastic hinges formed at the beam ends, the lateral stiffness of the model was positively correlated with the column stiffness: the initial stiffnesses of the CS-1, Base, CS-2, and CS-3 models were 4.74 kN/mm, 5.20 kN/mm, 5.49 kN/mm, and 5.74 kN/mm, respectively, representing increases of 9.9%, 20.3%, and 25.4% as the column stiffness increased from $0.5I_c$ to I_c, $2.0I_c$, and $2.83I_c$, respectively. Thus, the rate of increase in the initial stiffness of the model gradually slowed with increasing column stiffness. The stiffness degradation curves for all models basically overlapped after plastic hinges were formed at the beam ends, indicating that the influence of the column stiffness on the lateral stiffness of the model was negligible because the beam end sections no longer had the ability to resist bending moments. At this point, the steel frame can be simplified as a hinged frame with a lateral stiffness of 0, and as the lateral stiffness of the model was entirely provided by the CFSW, the stiffness of the columns had little effect.

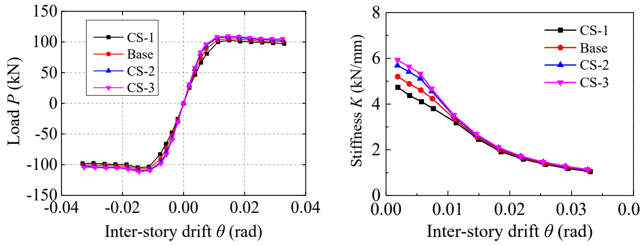

(a) (b)

Fig. 17 CS model series results: (a) skeleton curves; (b) stiffness degradation curves

Table 8
Characteristic values of CS model series skeleton curves

Model	Direction	Yield point		Peak point		Failure point	
		θ_y	P_y (kN)	θ_m	P_m (kN)	θ_u	P_u (kN)
CS-1	Positive	0.0076	80.9	0.0149	102.9	0.0330	97.2
	Negative	-0.0074	-82.7	-0.0150	-104.7	-0.0331	-98.1
Base	Positive	0.0075	88.9	0.0147	105.3	0.0327	100.9
	Negative	-0.0075	-90.9	-0.0148	-107.0	-0.0328	-100.5
CS-2	Positive	0.0072	93.2	0.0145	108.1	0.0325	103.1
	Negative	-0.0073	-95.5	-0.0146	-109.9	-0.0326	-102.2
CS-3	Positive	0.0073	96.2	0.0145	109.6	0.0325	105.4
	Negative	-0.0072	-97.2	-0.0146	-111.6	-0.0326	-104.6

5. Calculating the shear capacity of a single MSS-CFSW frame with semi-rigid connections

Wang et al. [7] analyzed the results of cyclic tests conducted on a single MSS-CFSW frame and observed no separation between the CFSW and steel frame. Thus, the connectors can provide a firm connection between the two components to effectively transmit forces. Based on the superposition method, the shear capacity P of a single frame with hinged boundary conditions can be assumed to comprise two parts: the shear capacity P_f of the single steel frame with hinged boundary conditions and the shear capacity P_w of the CFSW.

In modular steel structures, module units are connected using vertical inter-module semi-rigid connections that constrain the steel frame and improve the unit shear capacity. The shear capacity of a single MSS-CFSW frame considering semi-rigid connections is defined as P_{sr}. Similar to P, P_{sr} includes the shear capacity of a single steel frame with vertical inter-module semi-rigid connections $P_{f,sr}$ and the shear capacity of the CFSW P_w as follows:

$$P_{sr}=P_{f,sr}+P_w \tag{1}$$

Note that $P_{f,sr}$ considers the influence of the vertical inter-module semi-rigid connections, whereas because the CFSW is located inside the steel frame, P_w is unaffected by the vertical inter-module semi-rigid connections.

Referring to the calculation method for the shear capacity of a single steel frame with hinged boundary conditions presented in reference [7], the relationship between the bending moment amplitude and shear in the column section and equilibrium condition of forces can be used to obtain $P_{f,sr}$. The calculation diagram for a single steel frame with vertical inter-module semi-rigid connections is shown in Fig. 18, in which the semi-rigid connections at the tops and bottoms of the columns have been simplified as rotational springs [30]. When a lateral load F acts on the top of a column, the rotational springs rotate with the beam–column joints inside the module, inducing an interaction force between the two components. When conducting a force analysis, each rotational spring can be separated from the steel frame and a reaction moment M_r can be applied at the corresponding beam–column joint in its place. Therefore, the force state of a single steel frame with vertical inter-module semi-rigid connections under the action of F can be considered equivalent to the force state of a single steel frame with hinged boundary conditions under the simultaneous action of F and M_r, as shown in Fig. 18. Thus, the bending moment amplitudes of each section of a single steel frame with hinged boundary conditions must be obtained separately under the action of F and M_r, then superimposed.

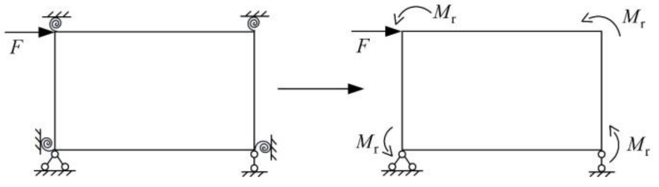

Fig. 18 Calculation diagram of a single steel frame with vertical inter-module semi-rigid connections

Under the action of F, the bending moment in each section reaches its maximum value when the single steel frame with hinged boundary conditions reaches its ultimate state. Strain data from the previous test were analyzed to determine that the single steel frame with hinged boundary conditions reached its ultimate state when part of the beam end section entered plasticity [7]. At this time, the lateral load applied to the single steel frame with hinged boundary conditions is P_f and the bending moments at the ends of the ceiling and floor beams are M_c and M_f, respectively, which can be calculated using Eqs. (28) and (29) in reference [7], respectively. The corresponding bending moment amplitude diagram can be obtained as shown in Fig. 19(a).

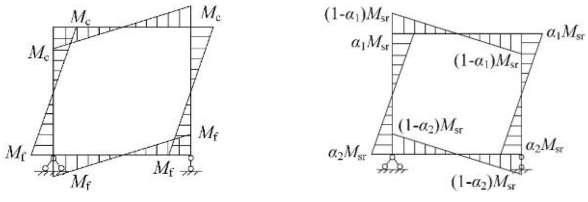

(a) (b)

Fig. 19 Bending moment diagram of a single steel frame with hinged boundary conditions: (a) under the action of P_f; (b) under the action of M_{sr}

The bending moment in each section reaches its maximum value when M_r is at its maximum. Thus, the maximum M_r represents the bending moment capacity M_{sr} of the vertical inter-module semi-rigid connection. Fig. 20 shows the calculation diagram for a single steel frame with vertical inter-module semi-rigid connections under the action of M_r, in which i_c, i_{b1}, and i_{b2} denote the linear stiffnesses of the column, ceiling beam, and floor beam, respectively. When the reaction bending moment M_{sr} is applied at joints A, B, C, and D, they will experience rotations θ_A, θ_B, θ_C, and θ_D. Based on the slope–deflection equations, the bending moments at the column and beam ends at joints A, B, C, and D can be respectively obtained by

$$M_{AB}=4i_{b1}\theta_A+2i_{b1}\theta_B \tag{2}$$

$$M_{AC}=4i_c\theta_A+2i_c\theta_C \tag{3}$$

$$M_{BA}=2i_{b1}\theta_A+4i_{b1}\theta_B \tag{4}$$

$$M_{BD}=4i_c\theta_B+2i_c\theta_D \tag{5}$$

$$M_{CD}=4i_{b2}\theta_C+2i_{b2}\theta_D \tag{6}$$

$$M_{CA}=2i_c\theta_A+4i_c\theta_C \tag{7}$$

$$M_{DC}=2i_{b2}\theta_C+4i_{b2}\theta_D \tag{8}$$

$$M_{DB}=2i_c\theta_B+4i_c\theta_D \tag{9}$$

where M_{AB} and M_{AC} are the bending moments at the end of ceiling beam AB and column AC at joint A, respectively; M_{BA} and M_{BD} are the bending moments at the end of ceiling beam AB and column BD at joint B, respectively; M_{CD} and M_{CA} are the bending moments at the end of floor beam CD and column AC at joint C, respectively; and M_{DC} and M_{DB} are the bending moments at the end of floor beam CD and column BD at joint D, respectively.

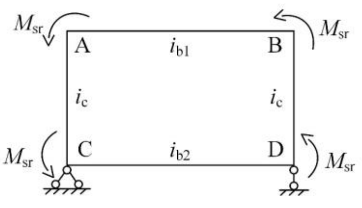

Fig. 20 Calculation diagram for a single steel frame with hinged boundary conditions under the action of M_{sr}

Based on the moments at joints A, B, C, and D, the following moment equilibrium equations can be established:

$$\begin{cases} M_{AB}+M_{AC}+M_{sr}=0 \\ M_{BA}+M_{BD}+M_{sr}=0 \\ M_{CA}+M_{CD}+M_{sr}=0 \\ M_{DB}+M_{DC}+M_{sr}=0 \end{cases} \tag{10}$$

Substituting Eqs. (2)–(9) into Eq. (10), rotations θ_A, θ_B, θ_C, and θ_D can be obtained and subsequently introduced into Eqs. (3) and (7) to derive the maximum bending moment at the top and bottom ends of column AC, respectively, as follows:

$$M_{AC}=-\frac{i_c\left(i_{b1}+2i_{b2}+i_c\right)}{3i_{b1}i_{b2}+\left(2i_{b1}+2i_{b2}+i_c\right)i_c}M_{sr} \tag{11}$$

$$M_{CA}=-\frac{i_c\left(2i_{b1}+i_{b2}+i_c\right)}{3i_{b1}i_{b2}+\left(2i_{b1}+2i_{b2}+i_c\right)i_c}M_{sr} \tag{12}$$

which can be regarded as products of moment distribution coefficients α_1 and α_2, respectively, and M_{sr}, as follows:

$$M_{AC}=-\alpha_1 M_{sr} \tag{13}$$

$$M_{\mathrm{CA}} = -\alpha_2 M_{\mathrm{sr}} \tag{14}$$

Where

$$\alpha_1 = \frac{i_{\mathrm{c}}\left(i_{\mathrm{b1}} + 2i_{\mathrm{b2}} + i_{\mathrm{c}}\right)}{3i_{\mathrm{b1}}i_{\mathrm{b2}} + \left(2i_{\mathrm{b1}} + 2i_{\mathrm{b2}} + i_{\mathrm{c}}\right)i_{\mathrm{c}}} \tag{15}$$

$$\alpha_2 = \frac{i_{\mathrm{c}}\left(2i_{\mathrm{b1}} + i_{\mathrm{b2}} + i_{\mathrm{c}}\right)}{3i_{\mathrm{b1}}i_{\mathrm{b2}} + \left(2i_{\mathrm{b1}} + 2i_{\mathrm{b2}} + i_{\mathrm{c}}\right)i_{\mathrm{c}}} \tag{16}$$

From the symmetry of the structure and load, the maximum bending moment in column BD can be assumed equal to that in column AC. By combining the moment equilibrium conditions of the joints, the maximum bending moment diagram for a single steel frame with hinged boundary conditions under the action of M_{sr} can be obtained as shown in Fig. 19(b). Based on Figs. 19(a) and (b), the maximum bending moment $M_{\mathrm{col,t}}$ at the column top section and maximum bending moment $M_{\mathrm{col,b}}$ at the column bottom section are respectively given by

$$M_{\mathrm{col,t}} = M_{\mathrm{c}} + \alpha_1 M_{\mathrm{sr}} \tag{17}$$

$$M_{\mathrm{col,b}} = M_{\mathrm{f}} + \alpha_2 M_{\mathrm{sr}} \tag{18}$$

The modular steel frame can be divided into upper and lower parts along the column center; the upper part is analyzed to establish the lateral force equilibrium equation. Considering the relationship between the maximum bending moment and shear in the column, the expression for $P_{\mathrm{f,sr}}$ can be obtained as

$$P_{\mathrm{f,sr}} = 2 \times \frac{\left(M_{\mathrm{col,t}} + M_{\mathrm{col,b}}\right)}{h} = \frac{2\left(M_{\mathrm{c}} + \alpha_1 M_{\mathrm{sr}} + M_{\mathrm{f}} + \alpha_2 M_{\mathrm{sr}}\right)}{h} \tag{19}$$

in which $\alpha_1 = \alpha_2 = 0$ when calculating the shear capacity of a single steel frame with hinged boundary conditions owing to the absence of constraint by semi-rigid connections.

When calculating the shear capacity P_{w} of the CFSW used in this study, Wang et al. [7] proposed four revisions to the conventional global analysis method to provide the modified global analysis method detailed in Section 6.1 of reference [7]. This method not only considers the presence of horizontal and vertical joints but also targets wallboard units that are more in line with the actual situation. The calculation of P_{w} is given as follows:

$$P_{\mathrm{w}} = \min\left\{P_1 + P_2 + P_3, P_4 + P_5 + P_6\right\} \tag{20}$$

where P_i is the shear capacity of wallboard unit i, as shown in reference [7].

Table 9 compares the theoretical and simulated shear capacities for each parametric analysis model, indicating that the ratios of the theoretical to simulated shear capacities were between 0.915 and 1.001 with an average value of 0.951 and a standard deviation of 0.023. Thus, the theoretical values agreed well with the simulated values, and the former were generally smaller. This confirms that the calculation method proposed in this paper can effectively determine the shear capacity of a single MSS-CFSW frame with hinged boundary conditions and semi-rigid connections.

The following process can be applied to design the shear capacity of modular steel structures using the derived equation: (1) Determine the type of inter-module connection to be used based on the design requirements. (2) Calculate the horizontal design load to be borne by the single modular steel structure frame. (3) Calculate the inter-module connection rotational stiffness and moment capacity based on the equations provided in the design codes. (4) Based on the preliminarily determined cross-sectional dimensions of the module unit, use the derived equations to calculate the horizontal load that a single frame can resist. If the calculated value is larger than the horizontal design load, the designed cross-sectional dimensions are feasible; otherwise, the cross-sectional dimensions must be improved until the calculated value is greater than the design load.

6. Conclusions

A refined FE model of a single MSS-CFSW frame was established using ABAQUS and the connector unit parameters were determined from the results of shear tests on self-drilling screw connections under shear perpendicular and parallel to the plate edge. The effectiveness of the refined FE modeling method was verified against previous test results, and the influences of the semi-rigid connection and steel frame component stiffnesses on the cyclic behavior of a single frame were investigated. Finally, the semi-rigid connection was considered equivalent to a rotational spring to derive an equation for the shear capacity of a single MSS-CFSW frame. The primary conclusions of this study are as follows:

(1) When the distance from the screws to the plate edge was small, the failure mode and shear capacity of the self-drilling screw connection differed according to the direction of shear (perpendicular or parallel to the plate edge). However, there was no such difference when the distance from the screws to the plate edge was large. In the refined FE model, values were assigned to connector unit parameters in both directions in the CFSW plane according to these results. The numerical simulation results agreed well with the test results.

(2) The connection rotational stiffness and moment capacity were positively correlated with the initial stiffness and shear capacity of the single MSS-CFSW frame, respectively. The maximum increase in initial stiffness was 31.5% and the positive and negative shear capacities increased by 20.2–79.4%. The semi-rigid connections only constrained the steel frame before yielding, after which their influence should not be considered.

(3) As the stiffnesses of the ceiling beam, floor beam, and column increased, the initial stiffness of the single MSS-CFSW frame increased by 8.1–25.8%, 9.7–21.1%, and 9.9–25.4%, respectively, and its shear capacity increased by 14.0–41.0%, 15.8–61.1%, and 2.2–6.5%, respectively. Thus, the influences of these three parameters on the initial stiffness were similar, whereas the floor beam stiffness had a more significant influence on the shear capacity than the other parameters.

(4) The shear capacity of a single MSS-CFSW frame with semi-rigid connections comprises the shear capacities of the steel frame and CFSW. By equating the semi-rigid connections to rotational springs, an equation was derived for the shear capacity of the frame that quantified the contributions of the semi-rigid connections using moment distribution coefficients. The shear capacity of the CFSW was calculated using a previously proposed equation. A comparison of theoretical and simulated values indicated that by calculating the moment distribution coefficient values, the proposed method can effectively determine the shear capacity of a single MSS-CFSW frame with semi-rigid connections or hinged boundary conditions.

Table 9
Comparison between theoretical and simulated shear capacities of parametric analysis models

Model	Direction	Theoretical value			P_{FE} (kN)	$P_{\mathrm{sr}}/P_{\mathrm{FE}}$
		$P_{\mathrm{f,sr}}$	P_{w}	P_{sr}		
Base	Positive	54.3	48.2	102.5	105.2	0.974
	Negative	54.3	48.2	102.5	107.0	0.958
CRS-1	Positive	91.9	48.2	140.1	145.0	0.966
	Negative	91.9	48.2	140.1	144.5	0.970
CRS-2	Positive	91.9	48.2	140.1	148.5	0.943
	Negative	91.9	48.2	140.1	150.1	0.933
CRS-3	Positive	91.9	48.2	140.1	148.5	0.943
	Negative	91.9	48.2	140.1	150.2	0.933

CMC-1	Positive	73.1	48.2	121.3	126.6	0.958
	Negative	73.1	48.2	121.3	128.6	0.943
CMC-2	Positive	91.9	48.2	140.1	149.5	0.937
	Negative	91.9	48.2	140.1	148.0	0.947
CMC-3	Positive	129.4	48.2	177.6	187.2	0.949
	Negative	129.4	48.2	177.6	187.8	0.946
CBS-1	Positive	43.7	48.2	91.9	92.1	0.998
	Negative	43.7	48.2	91.9	93.9	0.979
CBS-2	Positive	64.3	48.2	112.5	121.5	0.926
	Negative	64.3	48.2	112.5	123	0.915
CBS-3	Positive	75.2	48.2	123.4	129.9	0.950
	Negative	75.2	48.2	123.4	131.1	0.941
FBS-1	Positive	42.4	48.2	90.6	90.5	1.001
	Negative	42.4	48.2	90.6	92.4	0.981
FBS-2	Positive	73.4	48.2	121.6	128.9	0.943
	Negative	73.4	48.2	121.6	127.5	0.954
FBS-3	Positive	86.7	48.2	134.9	145.8	0.925
	Negative	86.7	48.2	134.9	144.3	0.935
CS-1	Positive	54.3	48.2	102.5	102.9	0.996
	Negative	54.3	48.2	102.5	104.7	0.979
CS-2	Positive	54.3	48.2	102.5	108.1	0.948
	Negative	54.3	48.2	102.5	109.9	0.933
CS-3	Positive	54.3	48.2	102.5	109.6	0.935
	Negative	54.3	48.2	102.5	111.6	0.918
Average						0.951
Standard deviation						0.023

Funding

This study was supported by the Fundamental Research Funds for the Central Universities, grant number XJ2023001801.

Declaration of competing interests

The authors have no conflicts of interest to declare.

References

[1] Zhang P., Design and Mechanical Properties of Multi-storey Steel Module Structure. Master's Dissertation, Tianjin University, Tianjin, 2016.

[2] Ding Y., Deng E.F., Zong L., Dai X.M., Lou N., Chen Y., "Experimental study on seismic performance of corrugated steel plate shear wall in modular container construction", Journal of Building Structures, 39, 110–118, 2018.

[3] Ding Y., Deng E.F., Zong L., Dai X.M., Lou N., Chen Y., "Cyclic tests on corrugated steel plate shear walls with openings in modularized-constructions", Journal of Constructional Steel Research, 138, 675–691, 2017.

[4] Dai X.M., Ding Y., Zong L., Deng E.F., Lou N., Chen Y., "Experimental study on seismic behavior of steel strip reinforced CSPSWs in modular building structures", Journal of Constructional Steel Research, 151, 228–237, 2018.

[5] Liu Y., Chen Z., Liu J., Bai Y., Zhong X., Wang X., "Lateral stiffness evaluation on corner-supported thin walled modular steel structures", Thin-Walled Structures, 157(6), 106967, 2020.

[6] Feng R., Liu S., Y. Qiu Y., "Seismic performance of multi-story modular box buildings, Journal Constructional Steel Research, 168, 106002, 2020.

[7] Wang Q., Su M., Deng Z., Chen R., Chen W., Zhou X., Gong H., Ma L., "Seismic performance and shear capacity of modular steel structures infilled with cold-formed steel walls using a novel connection system", Engineering Structures, 289, 116322, 2023.

[8] Wang Q., Su M., Chen R., Deng Z., Chen W., "Seismic performance and shear capacity of modular steel frames infilled with cold-formed steel walls with openings", Thin-Walled Structures, 187, 110744, 2023.

[9] Khan K., Chen Z.H., Liu J.D., Yan J.B., "Simplified modelling of novel non-welded joints for modular steel buildings", Advanced Steel Construction, 17(4), 412–424, 2021.

[10] Chen H.L., Ke C., Chen C., Li G.Q., "The tensile performance of inter-module connection with a bolt and shear key fitting for modular steel buildings", Advanced Steel Construction, 19(2), 102–111, 2023.

[11] Dai X.M., Zong L., Ding Y., Li Z.X., "Experimental study on seismic behavior of a novel plug-in self-lock joint for modular steel construction:", Engineering Structures, 181, 143–164, 2019.

[12] Lacey A.W., Chen W., Hao H., Bi K., "New interlocking inter-module connection for modular steel buildings: Experimental and numerical studies", Engineering Structures, 198, 109465, 2019.

[13] Sanches R., Mercan O., Roberts B., "Experimental investigations of vertical posttensioned connection for modular steel structures", Engineering Structures, 175, 776–789, 2018.

[14] Yang N., Xia J., Chang H., Zhang L., Yang H., "A novel plug-in self-locking inter-module connection for modular steel buildings", Thin-Walled Structures, 187, 110774, 2023.

[15] Chua Y.S, Liew J.R., Pang S.D., "Modelling of connections and lateral behavior of high-rise modular steel buildings", Journal of Constructional Steel Research, 166, 105901, 2020.

[16] Lacey A.W., Chen W., Hao H., Bi K., "Effect of inter-module connection stiffness on structural response of a modular steel building subjected to wind and earthquake load", Engineering Structures, 213, 110628, 2020.

[17] Wang Q., Su M., "Stability study on sway modular steel structures with semi-rigid connections", Thin-Walled Structures, 161, 107529, 2021.

[18] Huang Z.G., Seismic Behaviors Study on Low-Rise Cold-Formed Thin-Wall Steel Residential Buildings, PhD Dissertation, Xi'an University of Architecture and Technology, Xi'an, 2011.

[19] Xu Y., Experimental Research on Shear Performance of New-type Cold-formed Steel Load Bearing Walls, Master's Dissertation, Southeast University, Nanjing, 2016.

[20] Yu Q., Numerical Simulation on the Shear and Axial Compression Performance of Cold-Formed Steel Shear Walls, Master's Dissertation, Southeast University, Nanjing, 2016.

[21] Buonopane S.G., Bian G., Tun T.H., Schafer B.W., "Computationally efficient fastener-based models of cold-formed steel shear walls with wood sheathing", Journal of Constructional Steel Research, 110, 137–148, 2015.

[22] Hao J., Liu B., Shao D., Wang Y., Li K., Li Y., "Experimental study on shear behavior of screw connections in cold-formed thin-wall steel structures", Journal of Xi'an University of Architecture and Technology (Natural Science Edition), 46, 769–773+779, 2014.

[23] Li Y., Ma R., He H., "Experimental study on behavior of screw connections for cold-formed thin-walled steel and structural OSB boards", Journal of Building Structures, 35, 48–56, 2014.

[24] Ye J., Wang X., Zhao M., "Experimental study on shear behavior of screw connections in CFS sheathing", Journal of Constructional Steel Research, 121, 1–12, 2016.

[25] Han P., Experimental Study on Behavior of Screw Connections in CFS Keel-Sheeting Board, Master's Dissertation, Nanjing: Southeast University; 2018.

[26] Wang Q., Study on Seismic Performance of Semi-rigid Modular Steel Structure Filled with Cold-formed Steel Wall, PhD Dissertation, Xi'an University of Architecture and Technology, Xi'an, 2023.

[27] Zhao M., Behavior of Screw Connections in CFS-sheeting Board, Master's Dissertation, Southeast University, Nanjing, 2015.

[28] Huang R., Research on Hysteretic and Crack Resistance of Steel Frame-ALC Wallboard Structure System, Master's Dissertation, Harbin Institute of Technology, Harbin, 2021.

[29] GB 50017-2017, Standard for Design of Steel Structures, China Building Industry Press, Beijing, 2018.

[30] Wang Q., Su M., "Displacement mode of column-supported modular steel structures with semi-rigid connections", Journal of Building Engineering, 62, 105397, 2022.